



URANS-Based Prediction of Vortex Induced Vibrations of Circular Cylinders

E. Dobrucali¹ and O. K. Kinaci^{2,†}

¹ Turkish Naval Academy, Tuzla – Istanbul

² Yildiz Technical University, Besiktas – Istanbul

†Corresponding Author Email: kinaci@yildiz.edu.tr

(Received October 31, 2016; accepted January 24, 2017)

ABSTRACT

Vortex induced vibrations (VIV) are highly nonlinear due to three different frequencies involved in the process; fluid force frequency, vortex shedding frequency and oscillation frequency. It is computationally complex to solve such a chaotic fluid flow but recent progress in numerical algorithms, turbulence models and computer capabilities have made it easier to approach the problem with a nonlinear approach. These developments have paved the way to approach the problem with the simple equation of motion of Newton's law and when coupled with URANS, which is a commonly used method in solving problems related to fluid flow, the highly nonlinear problem of vortex induced vibrations become solvable. The existing literature computationally can only handle flows for $Re > 10,000 - 12,000$ but the numerical methodology adopted in this study furthers this limitation. The numerical algorithm is first tried for a stationary cylinder and the boundary layer separation is investigated for higher Re . The generated results are found to be satisfactory to proceed solving for VIV at high Re . The solution strategy is tested in a wide range of Reynolds number with different springs and damping coefficients. Satisfactory agreement is found with the experiments for a cylinder in VIV. The shortcomings of the computational work and why these limitations arise are tried to be explained using the experimental results and the existing mathematical models.

Keywords: VIV; Flow around cylinder; Reduced velocity; Oscillation frequency; Spring stiffness.

NOMENCLATURE

A	amplitude	U^*	reduced velocity
A^*	non-dimensional amplitude	y	displacement of the body
c	damping,	\dot{y}	vertical velocity of the body
C_l	lift coefficient	\ddot{y}	vertical acceleration of the body
D	diameter of the cylinder	ζ	damping coefficient,
F	fluid force	ζ_v	damping coefficient in vacuum,
f_s	strouhal frequency	ρ	fluid density
$f_{n,v}$	nat. freq. in vacuum,	ϕ	phase difference
$f_{n,w}$	nat. freq. in still water,		
f_{osc}	oscillation frequency		
f^*	non-dimensional frequency		
k	spring stiffness		
L	length of the cylinder		
m	oscillating mass		
m_a	added mass		
m_d	displaced mass		
m^*	mass ratio		
t	time		
Δt	time step size		
U_v^*	reduced velocity in vacuum		

Abbreviations

2D	two dimensional
3D	three dimensional
CFD	Computational fluid dynamics
CFL	Courant-Friedrich-Lewy
DOF	Degree-of-freedom
FSI	Fluid-structure interaction
FIM	Flow-induced motions
PTC	Passive turbulence control
Re	Reynolds number
SST	Shear stress transport
TrSL	Transition shear layer
URANS	Unsteady Reynolds-averaged Navier-

VIV	Stokes Eqns. Vortex-induced vibrations	VIVACE	Vortex-induced vibration for aquatic clean energy
-----	---	--------	---

1. INTRODUCTION

Engineering structures with bluff cross-sections, such as cylinders or slender structures and hydrofoils, airfoils, may originate alternating or oscillatory lift in uniform flows. When these structures are extensible or firm but mounted on flexible support, and have one or more natural frequencies of vibration in the range of frequencies of the oscillatory lift, significant flow-structure interaction (FSI) phenomena may be actuated (Blevins 2001 and Paidoussis *et al.* 2011). FSI are typically damaging phenomena in engineering applications. The potential destructive forces that can result from the interaction between a moving fluid and a structure were stunningly displayed in 1940 with the collapse of the Tacoma Narrows Bridge. In this manner, it has to be kept away from them by design or suppressed using excessive damping or appendages. If they are rather enhanced, flow-structure interaction may result in robust flow-induced motions (FIM) of the body. But then, bluff bodies such as circular cross-section cylinders may expose many forms of FIM that have been studied extensively but are still not well understood for suppression or enhancement. In its broadest sense, FIM can be divided into five. These are vortex-induced vibration (VIV) (Bearman 1984, Bernitsas *et al.* Gabbai and Benaroya 2005, Kumar *et al.* 2008, Sarpkaya 1979, Williamson and Govardhan 2004), galloping (Richardson *et al.* 1965, Chang *et al.* 2001), coexistence of VIV and galloping (Kim *et al.* 2013, Park *et al.* 2013, 2014), buffeting (Blevins 2001) and gap-flow in multi-body interaction (Assi *et al.* 2006 and 2010, Zdravkovich 1988, Zdravkovich and Medeiros 1991). This paper deals with only VIV of FIM.

The fluid separates from the body and an unsteady wake is originated as a fluid moves past a bluff body such as cylinder. This stimulates vortices to detach and shed from both sides of the body and be convected downstream by the flow. These shedding vortices generate periodic forces on the body. Generally, these forces are sufficiently strong to initiate the body into oscillatory motion. Such behavior is known as vortex-induced vibrations (VIV) and an immense number of structures are prone to VIV.

The studies regarding vortex induced vibrations of circular cylinders is very wide-ranging, and new conceptions are developed ceaselessly by using experiments (Klamo *et al.* 2005, Carberry 2001, Raghavan and Bernitsas 2011, Kim and Bernitsas 2016), field tests (Sumer and Fredsoe 1997), and numerical simulations (Williamson and Govardhan 2004, Juan *et al.* 2015, Ding *et al.* 2016, Kinaci *et al.* 2016a and b, Steven *et al.* 2016, Chung 2016, Jiang *et al.* 2016). Vortex-induced vibrations are highly nonlinear phenomena. The nonlinearity of the flow complicates mathematical models and it is harder to obtain results with high accuracy. Most of the

research in this field involved experimental science before common access to high speed computers became widespread. On the other hand, the swift technological progress in computational field has increased the capability of approaching the problem computationally in the last two decades. Some specific computational studies about latest research on VIV are investigated below.

Ding *et al.* (2016) investigated FIM of a single, rigid, circular cylinder on end-springs for $30,000 < Re < 110,000$. For harnessing marine hydrokinetic energy, passive turbulence control (PTC) in the form of roughness strips is applied to enhance FIM and raise the efficiency of the converter system named VIVACE (Vortex Induced Vibration for Aquatic Clean Energy). Numerical simulations are carried out by using a solver for two-dimensional Unsteady Reynolds-Averaged Navier-Stokes (2D-URANS) equations. The results are in partial agreement with experiments. Amplitude and frequency responses of the cylinder are in satisfactory accordance for all branches. In Kinaci *et al.* (2016a), selective local roughness is applied to the surface of a smooth circular cylinder to passively control the flow kinematics around the cylinder in a steady uniform flow. This method of changing the flow is called the Passive Turbulence Control (PTC). Application of PTC as a step on the cylinder returned satisfactory results with CFD in the TrSL3 flow regime. On the contrary, CFD results for smooth cylinders agree with experiments for lower Reynolds numbers only as Park *et al.* (2014) suggested although a subsequent study of Kinaci *et al.* (2016b) have shown that it is also possible to obtain good accordance with experimental results at even higher Reynolds numbers. Steven *et al.* (2016) investigated the flow around an elastically mounted cylinder using Large-Eddy Simulation (LES). 1DOF analysis of the heaving and torsional motions is carried out under a free vibration. Various characteristics of the flow-field at lock-in are discussed. Consequently, a divergence-free synthetic inflow generation approach is employed to analyze the effects of the free-stream turbulence on the bridge response.

Two-degree-of-freedom vortex induced vibration (VIV) of a low-mass zero-damping circular cylinder horizontally placed near a free surface at $Re = 100$ is numerically studied with an adaptive Cartesian cut-cell/level-set method in Chung (2016)'s study. The results show that the Froude number affects the critical normalized submergence depth and possible physical mechanisms are proposed. Jiang *et al.* (2016) investigated numerically VIV phenomena related to self-excited energy harvesters consisting of square cylinders by using the Bhatnagar–Gross–Krook (BGK) incompressible lattice Boltzmann method. The numerical results of the periodical and non-periodical oscillations and the frequency content

of the longitudinal and lateral forces acting on the square cross section harvester are discussed and validated by computing the flow around a fixed cylinder. The results are compared favorably with the results obtained by CFD methods. Juan *et al.* (2015) investigated numerically VIV on a circular cylinder with low mass-damping and low Reynolds number as basis for applications on dynamics of risers used in the offshore oil and gas industry. The results indicate the strong effect of the Reynolds number on the response amplitude, lift coefficient, and response frequency for a low mass-damping parameter. The upper branch of the response amplitude curve is only received when the Reynolds number varies proportionally to reduced velocity. Kinaci *et al.* (2016b) studied the effects of tip-flow on VIV experimentally and computationally. Computational results for VIV at these relatively high Reynolds numbers (up to 1.2×10^5) in the TrSL3 flow regime are not satisfactory. Their investigations showed that the tip-flow reduces the lift force exerted on the cylinder and narrows down the range of synchronization. As the Reynolds number increases, 2D computational simulations become inadequate to hold the effects of the tip-flow for a cylinder in VIV.

Considering the flow around a cylinder, either stationary or in VIV, free shear layers are formed close to the cylinder. Along the free shear layers, there are three phases of transition. The first one is the development of transition waves named TrSL1 ($350 - 400 < Re < 1,000 - 2,000$). The other is the formation of transition eddies named TrSL2 ($1,000 - 2,000 < Re < 20,000 - 40,000$). The last one of these phases is the turbulence phase named TrSL3 ($20,000 - 40,000 < Re < 100,000 - 200,000$). At the end of TrSL2, the finalization of the shortening of eddy formation region is accompanied by the disappearance of transition eddies in free shear layers. These incidents show the beginning of TrSL3. The transition to turbulence is reduced to a burst in free shear layers around the cylinder. The transition region comes out reluctant to progress upstream with increasing Re in TrSL3. The quasi-invariable nature of the flow in this regime is in sharp contrast to a continuous variation of the flow through all other flow regimes. The short eddy formation region produces a wide near wake. This displaces the free shear layers into the free stream and causes the acceleration of stream close to this near wake (Zdravkovich 1997).

Current research in this field is limited to flows that are $Re < 10,000$ for a cylinder in VIV and some works from the literature were briefly mentioned in the following sections. This paper focuses on a thorough URANS application of the problem for flows that are $Re > 10,000$ for smooth cylinders. The mathematical background, the implemented grid structure, the boundary conditions, the selection of turbulence model and the calculation of time step size were explained in detail. Numerical results were validated at TrSL2 flow regime first. Then the results were extended to cover TrSL3 flow regime for higher Re , making comparisons with experiments in a circulation channel to assess the suitability of the addressed numerical methodology.

2. MATHEMATICAL MODEL

The vibration equation of a cylinder attached with springs subjected to a fluid flow is given as;

$$m\ddot{y} + c\dot{y} + ky = F \tag{1}$$

where m represents the mass of the cylinder and $1/3$ of the spring mass, c represents the total mechanical damping and k the spring stiffness. F in equation (1) is the fluid force applied on the cylinder due to periodic vortex shedding from both sides of the cylinder surface.

The displacement y of the cylinder in time domain may be numerically solved at each time step discretizing y_{t+1} . It is given as;

$$y_{t+1} = y_t + \dot{y}_{t+1} \cdot \Delta t \tag{2}$$

where \dot{y} is the velocity of the cylinder and it is numerically represented as;

$$\dot{y}_{t+1} = \dot{y}_t + a_{t+1} \cdot \Delta t \tag{3}$$

Taking the first and second derivatives of the displacement y to obtain the velocity \dot{y} and the acceleration \ddot{y} , one can obtain the following equation to calculate the displacement versus time:

$$y_{t+1} = y_t + \dot{y}_t \Delta t + \left(\ddot{y}_t + \frac{F_{t+1} - c\dot{y}_t - ky_t}{m} \right) \cdot (\Delta t)^2 \tag{4}$$

Force F in equations (1-4) is calculated by the URANS approach at each time step. The calculated force is imposed on the cylinder to make a vertical displacement at that specific time step and this movement disturbs the flow in return. So it may be said that the computational approach to represent VIV involves a two-way fluid structure interaction (FSI) problem. The details of the computational approach are given in (Kinaci, 2016).

3. ANALYTICAL APPROACH

The linear mathematical model allows calculation of the lift coefficient exerted on the cylinder by the fluid; given the amplitude and the oscillation frequency. Algebraic transformation of equation (1):

$$m \left(\ddot{y} + \frac{c}{m} \dot{y} + \frac{k}{m} y \right) = F \tag{5}$$

Introducing the damping coefficient ζ_v and natural frequency $f_{n,v}$ (both in vacuum), the equation becomes:

$$m \left(\ddot{y} + 4\pi\zeta_v f_{n,v} \dot{y} + 4\pi^2 f_{n,v} y \right) = F \tag{6}$$

The force exerted on the cylinder is assumed to be sinusoidal in the linear approach. Taking into account the phase difference ϕ between the fluid force F and the oscillation frequency of the body f_{osc} , the force exerted on the body by the fluid may be represented by:

$$F = \frac{1}{2} \rho D L U^2 C_l \sin(2\pi f_{osc} t + \phi) \tag{7}$$

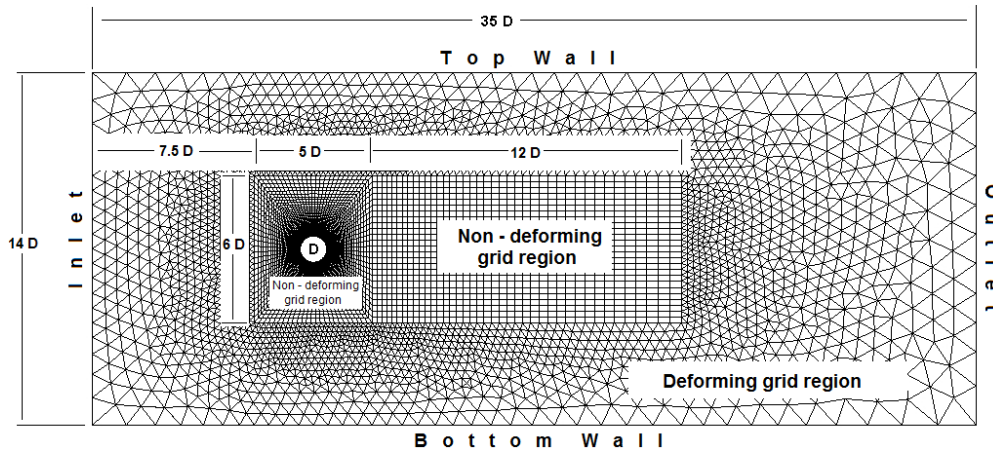


Fig. 1. Computational domain and its details.

Table 1 Boundary conditions of the computational domain

Boundary	Dimensions	Boundary condition	Moving?	Deforming?
Cylinder	D in diameter	Wall	Yes	No
Inlet	$14D$ in length	Velocity Inlet	No	No
Outlet	$14D$ in length	Pressure Outlet	No	No
Top Wall	$35D$ in length	Wall	No	No
Bottom Wall	$35D$ in length	Wall	No	No
Non-deforming region	$17D \times 6D$	Dynamic mesh	Yes	No
Deforming region	(Whole domain) -(Nondeforming region)	Static mesh	No	Yes

Assuming that the cylinder moves harmonically inside the fluid the displacement may be written as:

$$y = A \sin(2\pi f_{osc} t) \quad (8)$$

where A denotes the maximum amplitude in one cycle of oscillation. Solution of equation (6) with contributions from equations (7) and (8) will return two equations with two unknowns, C_l and ϕ :

$$C_l \cos(\phi) = \frac{2\pi^3 A^* m^* (1 - f^{*2})}{U_v^{*2}} \quad (9a)$$

$$C_l \sin(\phi) = \frac{4\pi^3 A^* m^* f^* \zeta_v}{U_v^{*2}} \quad (9b)$$

With this linear approach, which is extensively given in (Khalak and Williamson, 1999), the fluid force exerted on the cylinder and the phase difference between the oscillation and the fluid force can analytically be calculated with inputs provided by experiments. In this paper, evaluation of numerical results will be made by experiments where the lift coefficient on the cylinder is calculated analytically.

4. NUMERICAL APPROACH AND VALIDATION

The solution strategy implemented in this study along with the grid structure and turbulence model is briefly explained in this section. There is a validation

of the numerical approach with an experiment at TrSL2 flow regime which is regarded as a benchmark in the field of CFD applications in VIV.

All numerical simulations whose results are presented in this study are for 2D flows.

4.1. Grid Structure

The computational domain used in this study is briefly explained in this section and it is visually provided in fig. 1. A relatively old software Gambit 2.4.6 was used in setting up the grid system in the fluid domain which is considered to provide flexibility during meshing process.

The fluid domain consists of a two-dimensional rectangular block of dimensions $35D \times 14D$. The center of the cylinder of diameter D is taken as the origin. The cylinder is surrounded by a non-deforming grid region of dimensions $5D \times 6D$ with quad elements to reduce the number of elements and to obtain higher quality elements close to the cylinder boundaries. The same is applied to the wake region of dimensions $12D \times 6D$ and these two regions with non-deforming elements move together with the cylinder inside the deforming grid region. The deforming grid region covers the whole fluid domain except the two non-deforming grid regions and consists of triangular elements. The elements in this region are being re-meshed at each time step with respect to the cylinder's motions. The boundary conditions of the fluid domain are given in table 1.

4.2. Solution Strategy

The numerical approach implemented in this study uses Unsteady RANS (URANS) method, which is available in ANSYS Fluent 15.0, to solve the flow induced motion of a circular cylinder which is only free to move in the vertical direction. A rectangular box around the cylinder has an O-type structured grid which moves together with the cylinder inside the flow as explained in the previous section. Dynamic mesh system is implemented in the flow field which allows deformation of the unstructured grid system outside of the rectangular box surrounding the cylinder. There are a total of 12,000 elements in the domain initially but this number is prone to changes due to deformation of elements. While conducting the numerical simulations, it was noticed that at some cases, the number of elements reached 50,000 elements due to remeshing.

The steady flow around the stationary cylinder at the intended Re is solved first to maintain good initial values to start the transient flow. In the steady and the stationary cylinder case, there are no grid deformations so at this stage of the simulation, the elements are non-deforming throughout the whole fluid domain. This helps decreasing the required time for the simulations to converge. Then, a first order implicit transient formulation is selected to solve for the time-dependent nature of vortex-induced vibrations. SIMPLE algorithm is selected for the pressure-velocity coupling. Momentum, turbulent kinetic energy and specific dissipation rate all use the first order upwind scheme. A second order upwind scheme is also available but this scheme demands greater grid resolution and therefore a larger computer memory. It is considered to be practical to select the first order upwind scheme.

The selected dynamic meshing strategy forms the core of these types of simulations. An incompatible selection might lead to generation of nonphysical results. The dynamic mesh system implemented in this study works as follows:

- When the cylinder moves, the elements in the deforming grid region are compressed (or decompressed depending on their location in the domain) first. This stage is called smoothing.
- If the compression (or the decompression) of the elements are greater than a prescribed value, there is a risk that these elements might have skewness. This would corrupt the generated results and therefore they are detected at this stage.
- The detected elements that have the risk to have high skewness are divided into two (or sometimes more until the skewness is eliminated). This stage is called remeshing.

The time step size selection is based on the CFL condition and a minimum of 10 seconds of flow simulation is enough to achieve convergence of quantitative data like lift, drag, amplitude etc. It should be noted that in experiments 10 seconds of flow is insufficient to grasp the nature of the flow as the usual convention is to take measurements for at

least 60 seconds. However due to the implicit transient formulation, 10 seconds of the flow around the cylinder in VIV is not real-time. It is just needed to achieve convergence and due to the nature of URANS (the details of the turbulent fluctuations are not resolved), aspects like amplitude or lift do not deviate at each oscillation period. So when the numerical simulations implementing RANSE with implicit transient formulation reaches convergence, the achieved oscillation will continue forever. It is important to keep the residuals low at each time step to resolve the flow near the boundaries, so iterations per time step is selected to be 50.

A $k - \omega$ SST turbulence model is selected to introduce turbulent flow characteristics in the simulated flow. This turbulence model is considered to be the most suitable model for simulating flows around bluff bodies (Kinaci, 2016). The details of the turbulence model is presented in the next section.

4.3. $k - \omega$ SST Turbulence Model

The $k - \omega$ SST model (Menter, 1994) implemented in this study can be regarded as an advanced $k - \epsilon$ turbulence model. It is a hybrid model which also makes use of the standard $k - \omega$ turbulence model by transforming ϵ into ω by substituting $\epsilon = k\omega$ in the vicinity of wall boundaries to better resolve the boundary layer. Standard $k - \omega$ turbulence model is prone to producing large turbulence levels at the inlet and the outlet; therefore, initial values of k and ω have to be well specified. To overcome this problem, $k - \omega$ SST model switches to the standard $k - \epsilon$ outside the boundary layer. For further reading on the model, please refer to (Menter, 1994) and (Versteeg and Malalasekera, 2007).

By making use of both $k - \epsilon$ and $k - \omega$ turbulence models, $k - \omega$ SST model serves as a very useful option to solve for the adverse pressure gradients that a cylinder in VIV is very inclined to have. Due to the bluff geometry that the cylinder has, the boundary layer is somewhat curved and $k - \epsilon$ model shows poor performance in these conditions (Versteeg and Malalasekera, 2007). The adverse pressure gradients that is expected at the rear side of the cylinder cannot be modeled accurately by this model. On the other hand, to be able to fully take advantage of the $k - \omega$ SST model, grid resolution in the boundary layer region must be increased. Although this increases the computational load of the method, it is considered that the boundary layer separation on the cylinder will better be approximated.

4.4. Experimental Validation

Before moving on to present the generated results at higher Reynolds numbers (Re), the numerical approach is first validated with the experiments of Khalak and Williamson (1996) that is widely used as a benchmark in evaluating the validity of the computational studies. The results presented in (1996) are in low Re which covers the TrSL2 regime. Although the flow characteristics in this regime are inherently different than TrSL3 (which is the target flow regime in this study), it provides a good understanding of the level of the numerical accuracy implemented.

The results provided in fig. 2 are generated by implementing URANS with $k - \omega SST$ turbulence model which is considered to be the most suitable model for simulating flows around bluff bodies (Kinaci, 2016). This model is a combination of $k - \varepsilon$ and $k - \omega$ turbulence models and makes use of both models in appropriate places of the fluid domain. The details of the turbulence model was given in previous sections.

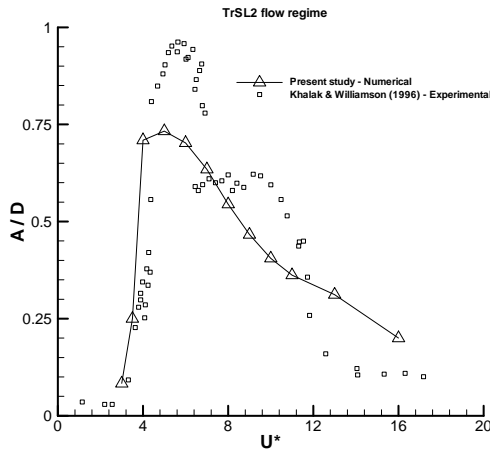


Fig. 2. Numerical results in comparison with experiments given in (Khalak and Williamson, 1996).

The numerical results generated in this study seem compatible with the experimental results of Khalak and Williamson (1996). The initial branch starts at $U^* = 4$ with a sudden jump in amplitude response at $U^* = 5$ both computationally and experimentally. The high amplitudes happening in the upper branch at $5 < U^* < 7$ are not very well captured with the numerical method implemented in this study which seems to be the major deficiency in the current approach. However; capturing the high amplitudes in the upper branch troubled the researchers working in this field for some time (Kinaci, 2016) and except a few exceptional studies (Wanderley *et al.*, 2008; Wu *et al.*, 2014) that partially capture the upper branch for some case studies, there is not a significant progress. The transition from the upper branch to lower branch is intermittent in Khalak and Williamson’s experiments but this transition is smoother computationally and results in a linear decrease in the amplitudes. There is a similar behavior in the desynchronization regime computationally as the decrease in the amplitude response continues linearly while it is sharper experimentally.

Vortex induced vibrations are highly non-linear and hard to approach with two-dimensional (2D) assumptions due to the chaotic nature of the flow. This complexity in the flow increases as the Re of the flow increases; therefore at these relatively high Re that is covered in this study, the validity of 2D numerical solutions decrease. Tip flow, cross flows and cellular shedding complicate the flow induced motions of the cylinder resulting in low accuracy of

the 2D simulations. This topic is investigated in detail in (Kinaci *et al.*, 2016b) and a numerical approximation to approach highly 3D flows with a 2D flow assumption is presented.

On the other hand, it is possible to approximate 2D flows in labs by extending the cylinder to the extents of the circulating channel as much as possible. It is of course impossible to fully make 2D experiments in labs, as the moving cylinder would be in touch with the walls of the lab setup which would disturb the flow induced motions. In this study, experimental results of a lab setup that approximates 2D flows will be used to compare the computational work carried out in this study (Lee and Bernitsas, 2011) in the next section. The distance between the tip of the cylinder and the channel walls is only 2% of the length of the cylinder and can be considered as a large end plate that enhances 2D flows.

5. STATIONARY CYLINDER CASE AT HIGH REYNOLDS NUMBERS

A stationary cylinder at a relatively high Re is investigated in this section as a preliminary study before moving on to solve the flow around a cylinder in oscillation. In some studies such as (Ding *et al.*, 2013; Wu *et al.*, 2014; Park *et al.*, 2014), it has been suggested that the boundary layer separation on a fixed cylinder at $Re > 10000 \sim 12000$ (some references say $Re > 20000$) cannot be predicted accurately which results in the failure of simulating numerically the smooth cylinders in VIV. Although this may partly be correct, it has been shown in this section that there is satisfactory accordance with experiments until the cylinder experiences drag crisis in the critical (near $Re > 3 \cdot 10^5$) and the super-critical (around $3 \cdot 10^5 < Re < 10^6$) regions.

The drag coefficient of a stationary cylinder between $10^4 < Re < 10^5$ is given in fig. 3 on the left. The experimental results of (Achenbach, 1968) suggest nearly a constant value for the drag coefficient at this flow regime which is around $C_D \cong 1 - 1.05$. The results generated computationally in this study suggest a monotonic decrease of the drag coefficient and they digress from the experimental results as the Re increases. The reason of this digression relies on the boundary layer separation point on the cylinder which starts diverging from the experiments given in fig. 3 on the right. It should be noted here that the computationally suggested boundary layer separation point on the cylinder is calculated by spotting the first reversed flow vector just over the cylinder surface.

The comparison of the wall shear stress distribution along the cylinder is given in fig. 4. Investigation of the wall shear stress distribution is a different way of assessing the boundary layer separation point but the results are in accordance with the separation points calculated by the first reversed flow vector. In fig. 4, the boundary layer separation point on top of the cylinder is given at $\theta^o = 89^o$ and $\theta^o = 255^o$ at the bottom. Fig. 3 suggests the boundary layer separation at $\theta^o = 96^o$ but this is a mean result of the separation. Due to the vortex shedding on the cylinder, the boundary layer separation point actually

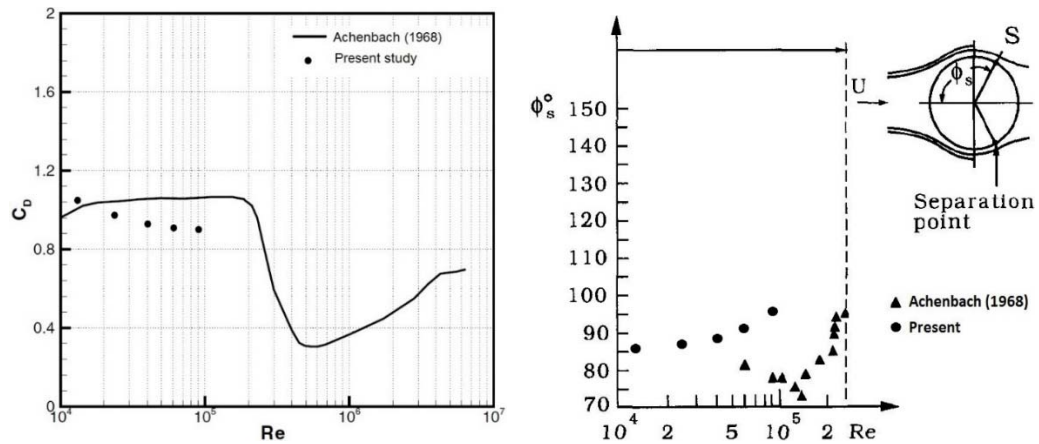


Fig. 3. Comparison of the drag coefficient obtained computationally in the present study and Achenbach’s experimental results (Achenbach, 1968) (left). Boundary layer separation point calculated computationally in contrast with (Achenbach, 1968) (right). Image taken and reproduced from (Sumer and Fredsoe, 1997).

moves between $88^\circ < \theta^\circ < 104^\circ$ so it may be said that the wall shear stress distribution given in fig. 4 is just taken after the vortex at the bottom of the cylinder is shed. The new vortex at the top of the cylinder just starts forming at this moment of the flow.

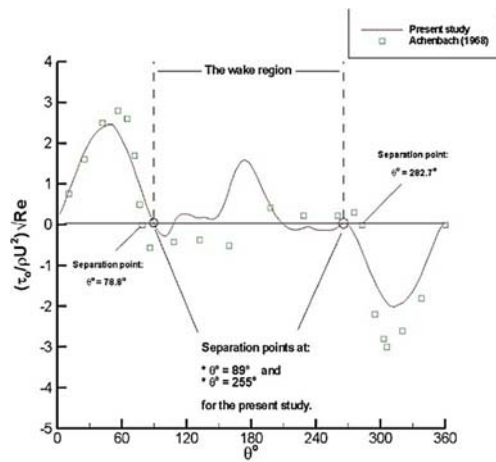


Fig. 4. Comparison of wall shear stress distribution with Achenbach (1968) for $Re = 10^5$.

Figure 4 reveals that there is accordance with the experimental results of (Achenbach, 1968) except the wake region. The separation points experimentally are about $\theta^\circ = 75^\circ$ and $\theta^\circ = 280^\circ$ which is $\theta^\circ = 89^\circ$ and $\theta^\circ = 255^\circ$ computationally and the stress distribution along the top and the bottom of the cylinder are in accordance. (It should also be noted here that we do not know for which specific moment in the flow Achenbach (1968) prepared this graph. The separation point moves back and forth on the cylinder with respect to periodic vortex shedding on the cylinder.) However the stress distribution in the wake region deviates from the experimental results but this is an expected result since it is

already known that URANS methods are insufficient to capture the wake mechanism of the cylinder (Sarpkaya, 2004). To better approximate the wake mechanism and the vortex structures forming in the fluid domain, Sarpkaya (2004) suggests more advanced numerical algorithms like LES.

Although the computational results get poorer with Re increasing as fig. 3 suggests, it cannot be said that the whole flow solution generated numerically overshoots the actual flow. To confirm this, a stationary cylinder at $Re = 10^6$ is numerically solved and the results are compared with the numerical results obtained by (Catalano *et al.*, 2003) at the same Re . Catalano *et al.* (2003) solved this flow with RANS, URANS and LES and made a comparison of these methods in terms of the pressure coefficient distribution on the cylinder given in fig. 5 on the left. They have stated that RANS fails to capture the pressure distribution on the cylinder so they suggest using URANS and LES to simulate the flow around a cylinder. The computational results of the present study are given in fig. 5 on the right and there is a satisfactory agreement with (Catalano *et al.*, 2003) except $170^\circ < \theta < 180^\circ$.

The streamwise velocity distribution of (Catalano *et al.*, 2003) obtained by URANS and LES and by URANS in the present study are given in fig. 6. The results of (Catalano *et al.*, 2003) suggest a shorter vortex length by LES and a longer one by URANS. The results of the present study show a similar behavior to the computational results generated by LES of (Catalano *et al.*, 2003).

6. RESULTS AND DISCUSSION

Using the numerical approach whose mathematical background is given in previous sections, the amplitude and frequency responses of the circular cylinder are calculated. The details of the grid dimensions and time step size are given in table 2.

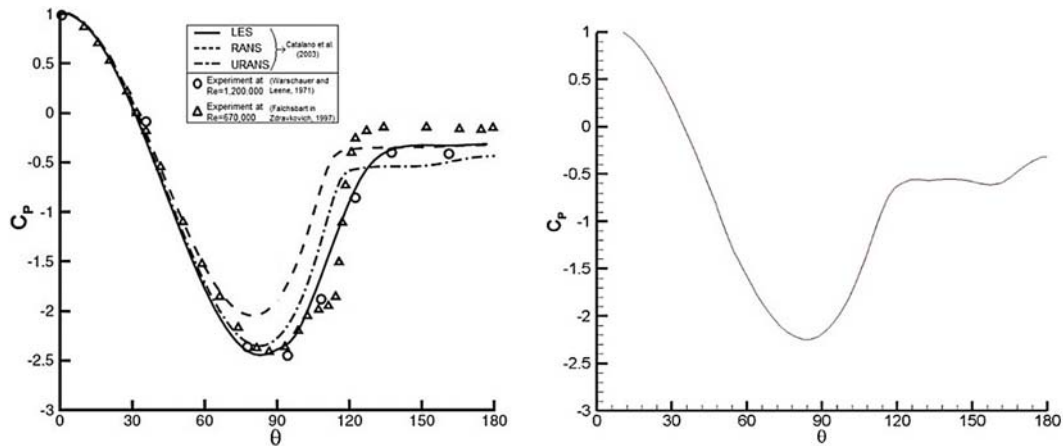


Fig. 5. Pressure coefficient distribution along the cylinder. Results of Catalano *et al.* (2003) by several computational methods (left). Present study obtained by URANS (right). $Re = 10^6$.

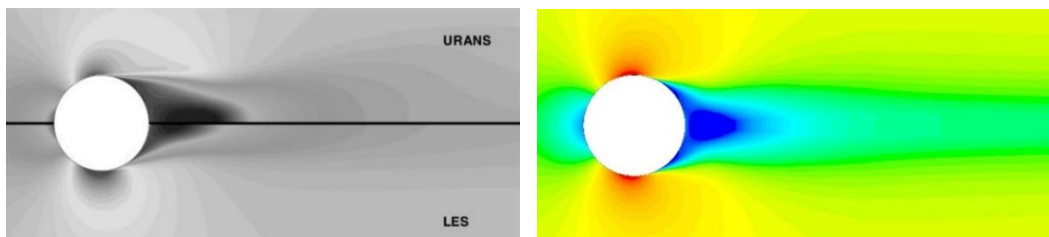


Fig. 6. Streamwise velocity distribution. Catalano *et al.* (2003) by URANS and LES (above). Present study by URANS (below). $Re = 10^6$.

Table 2 Details of the grid and time step size.

Property	Unit	Value
Cylinder diameter	m	0.0889
First cell length	m	0.0028
First cell thickness	m	0.0003
Time step size	s	0.0025

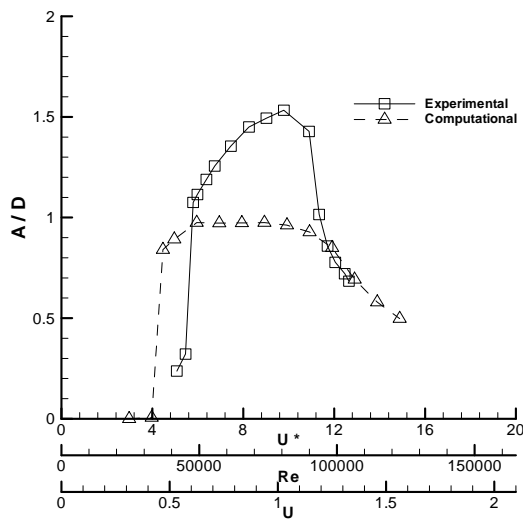


Fig. 7. Comparison of experimental (Lee & Bernitsas, 2011) and computational results of amplitude ratio vs. U^* , U , and Re for $k = 800 N/m$ and $\zeta_{tot} = 0.02$.

The mass ratio considered in this study is $m^* = 1.565$. Amplitude ratios versus current velocity (U), reduced velocity and Re for constant k and ζ_{tot} are given in fig. 7. The spring stiffness k and the harnessed damping ratio ζ_{har} are constant and they are $800N/m$ and 0 respectively. The structural damping, however, is not equal to zero and it is taken as a constant as per (Lee and Bernitsas, 2011). It is taken as $\zeta_{str} = 0.02$ to be compatible with the experiments of (Lee and Bernitsas, 2011). It can be seen that three main branches are available in this situation. The experimental results reveal that the initial branch occurs between $5 < U^* < 6$ while the numerical approach predicts earlier excitation of the cylinder which happens between $4 < U^* < 5$. The range of synchronization is wider computationally with a gradual change in the amplitude response while the experimental results show that there is a sharp increase in the amplitudes in the upper branch although the range of synchronization is narrower. The high amplitudes occurring in the experiments are not captured computationally as there is about 30% deficiency in the numerically generated results. This result is in accordance with the results obtained at lower Re in the previous section and is accounted to the simplifications in the turbulence models that URANS uses. Random behavior of the flow and its chaotic character plays an important role in getting the high amplitudes in the upper branch but URANS averages these random behaviors of the flow; restricting the maximum achieved amplitude. On the other hand the range of synchronization generated computationally and experimentally are compatible.

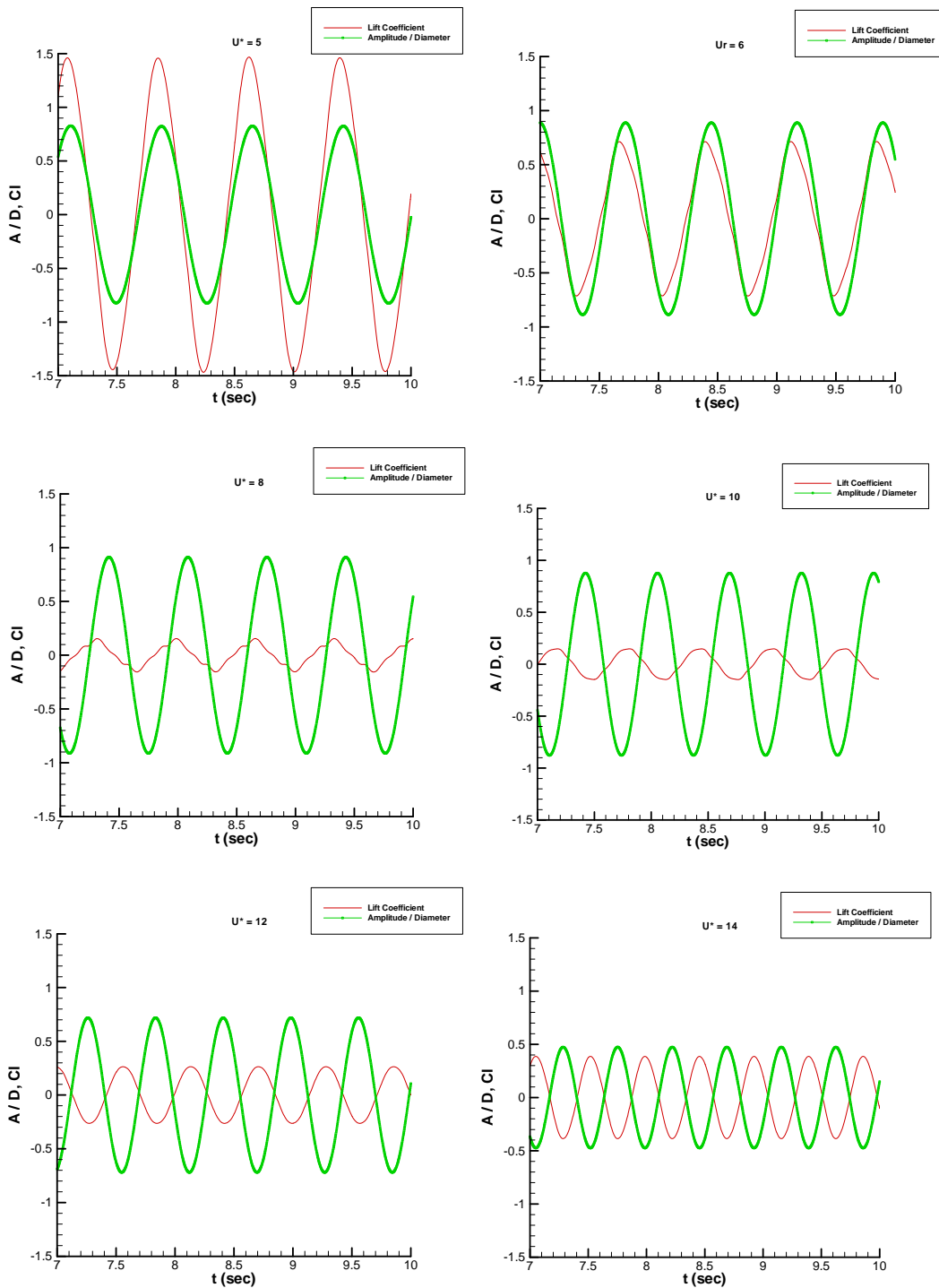


Fig. 8. Computationally generated amplitude response of the cylinder at different flow speeds vs. the fluid force.

This is accounted to the simplifications in the turbulence models that URANS uses. The lower branch which happens in the TrSL2 regime at lower Re is completely overtaken by the upper branch in the experiments. This is explained in detail in (Raghavan and Bernitsas, 2011) and is accounted to the Re effect on VIV. Computational results also suggest the nonexistence of the lower branch as there is a linear decrease in the generated amplitudes after

the upper branch. Both the results of the CFD and the experiments show that the oscillating cylinder goes into de-synchronization with the flow after $U^* > 12$.

The time versus force and displacement at various reduced velocities were investigated to understand the nature of VIV at different flow speeds and make sense of what all these branches identify. Fig. 8 presents the amplitude response of the cylinder

versus the force applied on the cylinder by the fluid at;

- $U^* = 5$ which is the end of the initial branch,
- $U^* = 6$ which is the start of the upper branch,
- $U^* = 8$ which is the at the upper branch,
- $U^* = 10$ which is the end of the upper branch,
- $U^* = 12$ and $U^* = 14$ which are at the de-synchronization regime.

The force generated by the fluid on the cylinder is the highest at $U^* = 5$ although the achieved amplitude is not the highest. This is a typical response of the initial branch and at these flow speeds the high fluid force starts exciting the cylinder. The fluid force drops at the upper branch as can be seen at $U^* = 6$ and even more at $U^* = 8$ but the amplitude is higher compared to the initial branch. The fluid force is in synchronization with the cylinder oscillation at all these reduced velocities; however starting from $U^* = 10$, they are not working together anymore. This reflects as a slight decrease in the amplitude response at $U^* = 10$ and the amplitudes continue to decline at $U^* = 12$ and $U^* = 14$ which can be seen in fig. 7. The fluid force and the cylinder is in desynchronization at $U^* = 12$ and $U^* = 14$ but the reason of lower achieved amplitude compared to $U^* = 10$ is due to the higher fluid force which absorbs the oscillation of the cylinder.

Figure 8 partially reveals the increase in the frequency response with respect to increasing flow speed. The frequency response versus the reduced velocity is shown in fig. 9. The frequency ratio curve of the present numerical results shows a clear increasing trend as the flow velocity increases in the range $30000 < Re < 114000$. The computational results follow a similar trend with the experiments although they are somewhat higher.

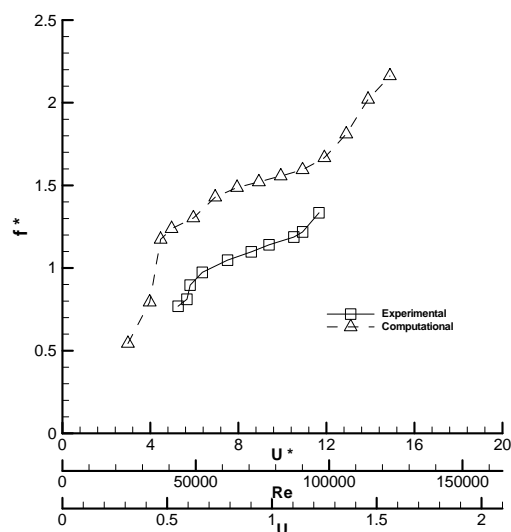


Fig. 9. Comparison of experimental (Lee & Bernitsas, 2011) and computational results of frequency ratio vs. U^* , U , and Re for $k = 800 \text{ N/m}$ and $\zeta_{tot} = 0.02$.

As is apparent in figs. 8 and 9, there is a lock-in region between $5 - 6 < U^* < 12$ which is partially captured numerically. The lift force provided by the fluid works together with the oscillation of the cylinder, supporting it to achieve higher amplitudes. Outside of this range, the cylinder is not totally in synchronization with the lift force and the amplitudes are limited. This phase difference between the oscillation and the lift force marks the boundaries of the branches in VIV which is extensively investigated in (Govardhan and Williamson, 2000).

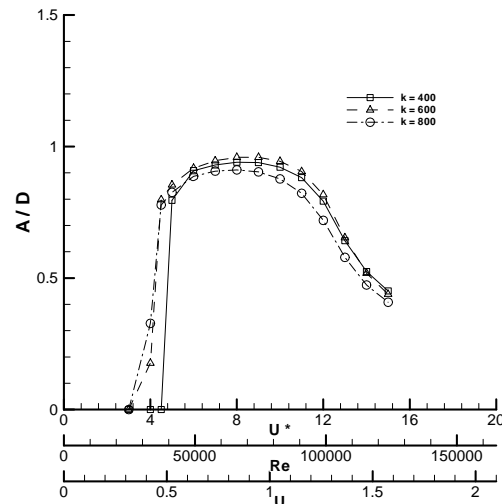


Fig. 10. Computationally generated amplitude ratios for $\zeta_{tot} = 0.02$ for various values of k .

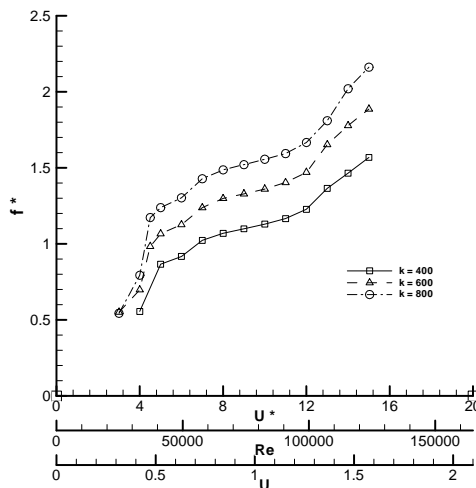


Fig. 11. Computationally generated frequency ratios for $\zeta_{tot} = 0.02$ for various values of k .

Figure 10 and fig. 11 reveal the amplitude and frequency response of the cylinder in VIV, highlighting the effect of spring stiffness. Higher spring stiffness results in higher natural frequency in still water (please refer to nomenclature for the equation). As k or $f_{n,w}$ increases, computational results suggest that the excitation (or in other words; the initial branch) starts earlier. The range of synchronization and the maximum achieved amplitude are not affected that much with the change

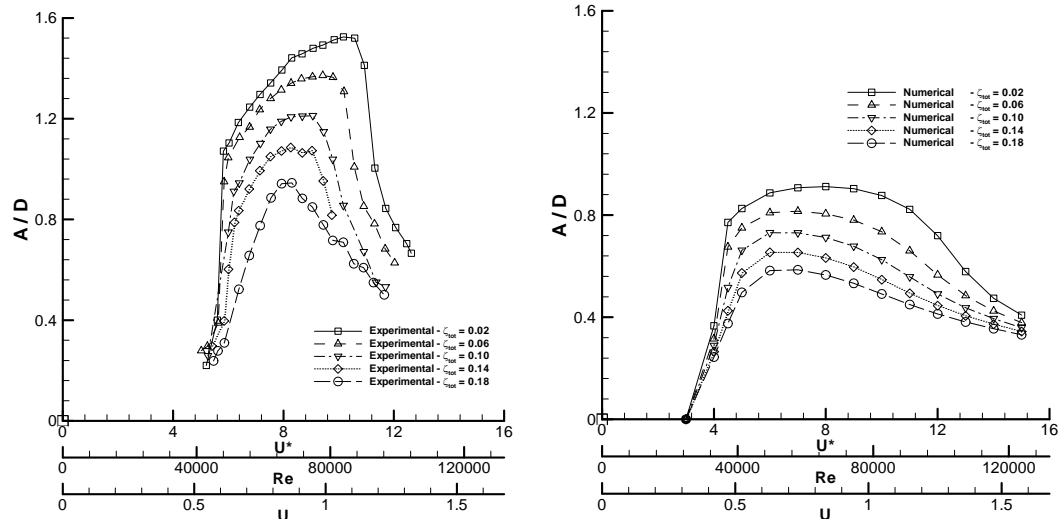


Fig. 12. Experimentally (left) (Lee and Bernitsas, 2011) and numerically (right) generated A^* vs. U^* , U , and Re for $k = 800 \text{ N/m}$ and various values of ζ_{tot} .

in the spring stiffness; although experimental results in (Lee and Bernitsas, 2011) suggest otherwise. This is one of the drawbacks of the computational model as some flow characteristics are not well captured with the suggested numerical simulation. Higher spring stiffness also results in higher frequency of the cylinder as presented in the frequency response of the cylinder in VIV in fig. 11.

Figure 12 presents the damping effect on VIV experimentally and numerically. The additional damping introduced to a cylinder in VIV suppresses the motions and restricts the amplitude. Both results show a decrease in the amplitude response at all reduced velocities. Another effect of damping is that it narrows down the range of synchronization. The upper branch occurs between $6 < U^* < 11$ for $\zeta_{tot} = 0.02$ while it is only happening at around $U^* \approx 8$ for $\zeta_{tot} = 0.18$. These results are in accordance with the linear mathematical theory. Fig. 13 is reproduced from the book by French (1971) and it shows the change in the amplitude response with the change in the damping. In that figure, horizontal axis is a form of frequency while the vertical axis is a form of the amplitude. Q is a term related to the inverse of the damping and named as “quality”. Lower Q means higher damping and therefore, the graphs given in fig. 12 and figure 13 are considered to be in accordance. For a better explanation on how the graph given in fig. 13 is obtained, please refer to (French, 1971).

The frequency response with a change in the damping is given in fig. 14. In that figure, it is directly noticeable that the computationally derived frequencies are higher when compared to the experimentally derived results. Other than the difference in the digital values between the computations and experiments, the general trends of the curves agree. Higher damping results in lower frequency before mid-upper branch while it is vice versa after the mid-upper branch. Experimental

results suggest that after $U^* < 9$, lower damping results in lower frequency while computationally this happens after $U^* < 7$.

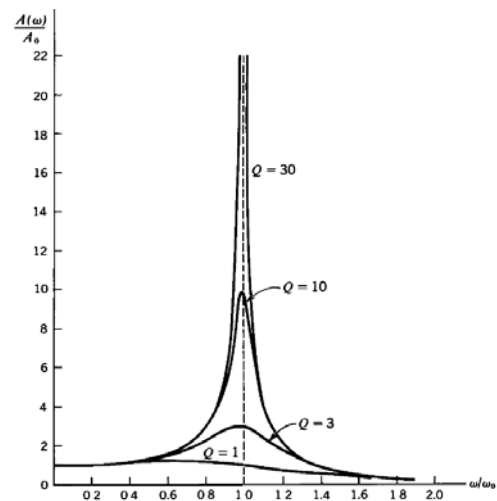


Fig. 13. Mathematically derived amplitude response showing the effect of damping with a linear approach taken from (French, 1971).

The final investigation in this paper is on what the computational method misses to show good agreement with the experiments. To understand what happens, fluid force applied on the cylinder is investigated at each U^* and this is given in fig. 15. The numerical results are derived from CFD while for the experimental results linear mathematical approach, which is presented in Section 3, is used. The graph helps understanding why, in fig. 2, the initial branch starts earlier computationally when compared with the experiments. The lift coefficients calculated by CFD make peak earlier when compared with the experiments and this results in earlier

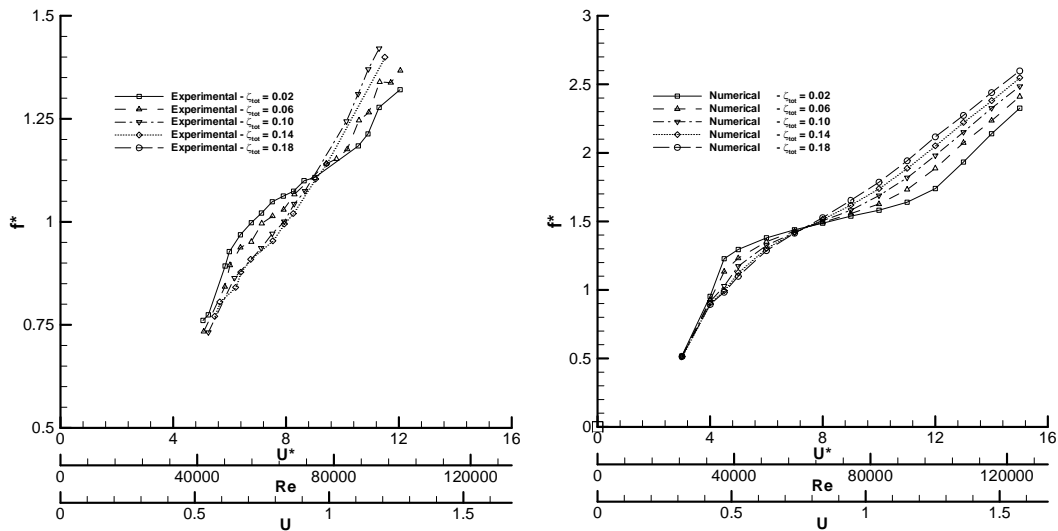


Fig. 14. Experimentally (left) (Lee and Bernitsas, 2011) and numerically (right) generated f^* vs. U^* , U , and Re for $k = 800 N/m$ and various values of ζ_{tot} .

excitation of the cylinder. Another discrepancy is that the computationally generated lift coefficients are lower at the upper branch which explains why the computational results are smaller with respect to the experimental results.

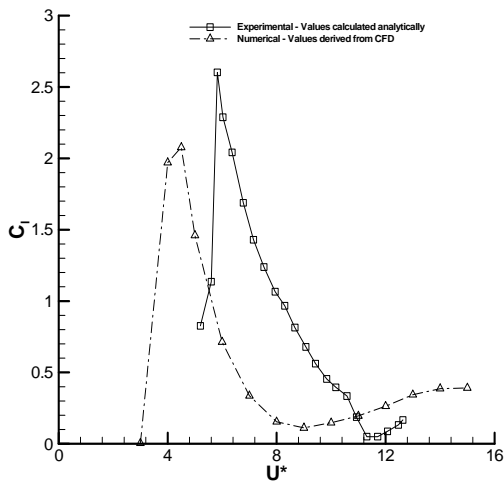


Fig. 15. Comparison of lift coefficients on the cylinder obtained computationally and experimentally (via linear mathematical approach) from (Lee and Bernitsas, 2011).

7. CONCLUSIONS

In this paper, an URANS based approach was presented to solve for the vortex induced vibrations of a circular cylinder. The numerical approach was first validated at TrSL2 flow regime of which many numerical and experimental results are available in the literature. Before extending for the TrSL3 regime, a stationary cylinder case at $Re > 10,000$ was investigated to evaluate if the solution strategy followed in this paper was able to capture the

boundary layer separation accurately. The results for the stationary cylinder was in accordance with the experimental and the other computational results that were already available in the literature. Then, the results were extended for higher Reynolds numbers to cover TrSL3 flow regime where the numerical results are limited. Many flow characteristics were captured with the numerical approach like the initial branch, range of synchronization, the desynchronization regime and the frequency and the amplitude responses of the cylinder. However, some other aspects like the high amplitudes occurring at the upper branch or the frequencies in the whole flow regime were not well calculated. The deficiencies and the limitations of the method were tried to be explained using the existing experiments in the literature or available linear mathematical models to set the scope of the suggested approach. These shortcomings of the method are expected to be solved in future studies with flow visualization tools offered by CFD softwares and making comparisons with experiments.

ACKNOWLEDGMENTS

This research has been supported in part by Yildiz Technical University Scientific Research Projects Coordination Department. Project No: 2015-10-01-GEP01.

REFERENCES

- Achenbach, E. (1968). Distribution of local pressure and skin friction around a circular cylinder in cross-flow up to $Re = 5 \times 10^5$. *Journal of Fluid Mechanics*, 34(4):625-639.
- Assi, G. R. S., Bearman, P. W., Meneghini and J. R. (2010). On the wake-induced vibration of tandem circular cylinders: the vortex interaction excitation mechanism, *Journal of Fluid Mechanics* 661, 365–401.

- Assi, G. R. S., J. R. Meneghini, J. A. P. Aranha, P. W. Bearman and E. Casaprima (2006). Experimental Investigation of Flow-Induced Vibration Interference Between Two Circular Cylinders, *Journal of Fluids and Structures* 22, 819–827.
- Bearman, P. (1984) Vortex shedding from oscillating bluff bodies, *Annual Review of Fluid Mechanics* 16, 195-222.
- Bernitsas, M. M., K. Raghavan, Y. Ben Simon and E. M. H. Garcia (2006 and 2008) VIVACE (Vortex Induced Vibration Aquatic Clean Energy): A New Concept in Generation of Clean and Renewable Energy from Fluid Flow, *OMAE and Journal of Offshore Mechanics and Arctic Engineering*, ASME Transactions 130(4), 041101-15.
- Blevins, R. D. (2001). Flow-Induced Vibration, *Krieger Publishing Co.* Malabar, Florida.
- Carberry, J. (2001). Wake States of a Submerged Oscillating Cylinder and of a Cylinder Beneath a Free Surface, *Ph.D thesis*, Monash University, Australia.
- Catalano, P., M. Wang, G. Iaccarino and P. Moin (2003). Numerical simulation of the flow around a circular cylinder at high Reynolds numbers, *International Journal of Heat and Fluid Flow*, 24, 463-469.
- Chang, C. C., R. A. Kumar and M. M. Bernitsas (2011). VIV and Galloping of Single Circular Cylinder with Surface Roughness at $3.0 \times 10^4 \leq Re \leq 1.2 \times 10^5$, *Ocean Engineering*, 38 1713-1732.
- Chung M. H. (2016). Two degree of freedom vortex induced vibration of low-mass horizontal circular cylinder near a free surface at low Reynolds number, *International Journal of Heat and Fluid Flow*, 57, 58-78.
- Ding, L., M. M. Bernitsas and E. S. Kim (2013). 2-D URANS vs. experiments of flow induced motions of two circular cylinders in tandem with passive turbulence control for $30,000 < Re < 105,000$, *Ocean Engineering*, 72, 429-440.
- Ding, L., L. Zhang, C. C. Chang and M. M. Bernitsas (2016). Numerical Simulation and Experimental Validation for Energy Harvesting of Single-Cylinder VIVACE Converter with Passive Turbulence Control, *Journal of Renewable Energy*, 85, 1246-1259.
- French, A. P. (1971). Vibrations and Waves, *The M.I.T Introductory Physics Series*, New York.
- Gabbai, R. and D. Benaroya (2005) An Overview of Modeling and Experiments of Vortex-Induced Vibration of Circular Cylinders, *Journal of Sound and Vibration*, 282 575-616.
- Govardhan, R. and C. H. K. Williamson (2000) Modes of vortex formation and frequency response of a freely vibrating cylinder, *Journal of Fluid Mechanics*, 420, 85-130.
- Jiang, X., Y. Andreopoulos T. Lee and Z. Wang (2016). Numerical investigations on the vortex-induced vibration of moving square cylinder by using incompressible lattice Boltzmann method, *Computers and Fluids*, 124, 270-277.
- Juan, B. V. W. and L. F. N. Soares (2015). Vortex-induced vibration on a two-dimensional circular cylinder with low Reynolds number and low mass-damping parameter, *Ocean Engineering*, 97, 156-164.
- Khalak, A. and C. Williamson (1996). Dynamics of a hydroelastic cylinder with very low mass and damping. *Journal of Fluids and Structures* 10, 455-472.
- Khalak, A. and C. H. K. Williamson (1999) Motions, forces and mode transitions in vortex-induced vibrations at low mass damping. *Journal of Fluids and Structures*, 13, 813-851.
- Kim, E. S. and M. M. Bernitsas (2016). Performance prediction of horizontal hydrokinetic energy converter using multiple-cylinder synergy in flow induced motion, *Applied Energy*, 170, 92-100.
- Kim, E. S., M. M. Bernitsas and A. R. Kumar (2013). Multi-Cylinder Flow Induced Motions: Enhancement by Passive Turbulence Control at $28,000 < Re < 120,000$, Proceedings of the 30th OMAE (2011) Conf., Paper #49405, Rotterdam, The Netherlands, June 19-24, 2011; and *Journal of Offshore Mechanics and Arctic Engineering*, ASME Transactions 135 (1).
- Kinaci, O. K. (2016). 2-D URANS simulations of vortex induced vibrations of circular cylinder at TrSL3 flow regime. *Journal of Applied Fluid Mechanics*, 9(5), 2537-2544.
- Kinaci, O. K., S. Lakka, H. Sun and M. M. Bernitsas (2016b). Effect of tip-flow on vortex induced vibration of circular cylinders for $Re < 1.2 \times 10^5$, *Ocean Engineering*, 117 130-142.
- Kinaci, O. K., S. Lakka, H. Sun, E. Fassezke and M. M. Bernitsas, (2016a). Computational and Experimental Assessment of Turbulence Stimulation on Flow Induced Motion of Circular Cylinder. *Journal of Offshore Mechanics and Arctic Engineering*, 138(4), 041802.
- Klamo, J. T., A. Leonard and A. Roshko (2005). On the Maximum Amplitude for a freely Vibrating Cylinder in Cross-Flow, *J. Fluids Struct.*, 21, 429–434.
- Kumar, R. A., C. H. Sohn, B. H. L. Gowda (2008). Passive Control of Vortex-Induced Vibrations: An Overview, *Recent Patents on Mechanical Engineering*, 1, 1-11.
- Lee, J. H. and M. M. Bernitsas (2011). High-damping, high-Reynolds VIV tests for Energy harnessing using the VIVACE converter, *Ocean Engineering*, 38, 1697–1712.
- Menter, F. (1994). Two-equation eddy-viscosity turbulence models for engineering applications. *AIAA Journal*, 1598-1605.

- Paidoussis, M. P., S. J. Price and E. DeLangre (2011) Fluid-Structure Interactions, *Cambridge University Press*. 13-25.
- Park, H. R., M. M. Bernitsas and C.C. Chang (2013). Robustness of the Map of Passive Turbulence Control to Flow-Induced Motions for a Circular Cylinder at $30,000 < \text{Re} < 120,000$, *Proceedings of the 31st OMAE 2013 Conf., Paper #10123*, Nantes, France, June 9-14.
- Park, H. R., M. M. Bernitsas and E. S. Kim (2014). Selective Surface Roughness to Suppress Flow-Induced Motions of Two Circular Cylinders at $30,000 < \text{Re} < 120,000$, *Proceedings of the 31st OMAE 2013 Conf., Paper #10125*, Nantes, France, June 9-14, (2013) *Journal of Offshore Mechanics and Arctic Engineering*, ASME Transactions 136-4.
- Raghavan, K. and M. M. Bernitsas (2011). Experimental investigation of Reynolds number effect on vortex induced vibration of rigid circular cylinder on elastic supports, *Ocean Engineering* 38, 719-731.
- Richardson, A. S., J. R. Martucelli and W. S. Price (1965) Research study on galloping of electric power transmission lines, *National Physics Lab Symposium H.M.S.O.*
- Sarpkaya, T. (1979) Vortex-induced oscillations: a selective review, *Journal of Applied Mechanics* 46, 241-257.
- Sarpkaya, T. (2004). A critical review of the intrinsic nature of vortex-induced vibrations. *Journal of Fluids and Structures* 389-447.
- Steven, J. D., I. P. Castro and X. Zheng Tong (2016). Numerical analysis of freestream Turbulence effects on the vortex-induced vibrations of a rectangular cylinder, *Journal of Wind Engineering and Industrial Aerodynamics*, 153, 13-25.
- Sumer, B. M. and J. Fredsoe (1997). Hydrodynamics Around Cylindrical Structures, *World Scientific, Singapore*.
- Versteeg, H. K. and W. Malalasekera (2007). An introduction to computational fluid dynamics—the finite volume method. *Harlow: Pearson Education Limited*.
- Wanderley, B., G. Souza and S. Sphaier (2008). Vortex-induced vibration of an elastically mounted circular cylinder using an upwind TVD two-dimensional numerical scheme, *Ocean Engineering*, 35, 1533-1544.
- Williamson, C. H. K. and R. Govardhan (2004) Vortex-induced vibrations, *Annual Review of Fluid Mechanics* 36, 413-455.
- Wu, W., M. M. Bernitsas and K. Maki (2014). RANS simulation versus experiments of flow induced motion of circular cylinder with passive turbulence control at $35,000 < \text{Re} < 130,000$, *Journal of Offshore Mechanics and Arctic Engineering*, 136(4), 041802-1-041802-10
- Zdravkovich, M. M. (1988). Review of Interference Induced Oscillations in Flow Past Two Parallel Circular Cylinders in Various Arrangements, *Journal of Wind Engineering and Industrial Aerodynamics* 28, 183-200.
- Zdravkovich, M. M., (1997). Flow Around circular cylinders: Volume 1, Oxford University Press.
- Zdravkovich, M. M. and E. B. Medeiros (1991). Effect of damping on interference-induced oscillations of two identical circular cylinders, *Journal of Wind Engineering and Industrial Aerodynamics* 38, 197-211.